# LANGMUIR

pubs.acs.org/Langmuir Article

# Mechanical Adaptability of Patterns in Constrained Hydrogel Membranes

Yao Xiong and Olga Kuksenok\*



Cite This: Langmuir 2021, 37, 4900-4912



**ACCESS** 

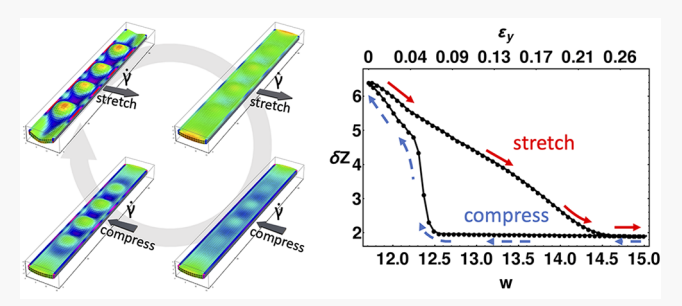
Metrics & More

□ Ar

Article Recommendations

Supporting Information

**ABSTRACT:** Pattern formation and dynamic restructuring play a vital role in a plethora of natural processes. Understanding and controlling pattern formation in soft synthetic materials is important for imparting a range of biomimetic functionalities. Using a three-dimensional gel Lattice spring model, we focus on the dynamics of pattern formation and restructuring in thin thermoresponsive poly(*N*-isopropylacrylamide) membranes under mechanical forcing via stretching and compression. A mechanical instability due to the constrained swelling of a polymer network in response to the temperature quench results in out-of-plane buckling of these membranes. The depth of the temperature



quench and applied mechanical forcing affect the onset of buckling and postbuckling dynamics. We characterize formation and restructuring of buckling patterns under the stretching and compression by calculating the wavelength and the amplitude of these patterns. We demonstrate dynamic restructuring of the patterns under mechanical forcing and characterize the hysteresis behavior. Our findings show that in the range of the strain rates probed, the wavelength prescribed during the compression remains constant and independent of the sample widths, while the amplitude is regulated dynamically. We demonstrate that significantly smaller wavelengths can be prescribed and sustained dynamically than those achieved in equilibrium in the same systems. We show that an effective membrane thickness may decrease upon compression due to the out-of-plane deformations and pattern restructuring. Our findings point out that mechanical forcing can be harnessed to control the onset of buckling, postbuckling dynamics, and hysteresis phenomena in gel-based systems, introducing novel means of tailoring the functionality of soft structured surfaces and interfaces.

# INTRODUCTION

Pattern formation and dynamic restructuring under external stresses exerted by the confinements play a critical role in a number of processes in nature. For example, compressive stresses generated by the smooth muscle control the transitions between the types of patterns—from longitudinal ridges to villi—in the lining of the human gut, while many features of phyllotactic patterns in plants can be understood by analyzing mechanical stability of growing elastic sheets undergoing buckling under lateral constraints.<sup>2–4</sup> Mechanical instabilities are triggered by sufficiently high compressive stresses, which may arise during growth, expansion, or swelling of soft layers or films under various geometrical constraints. 5-7 Specific patterns observed, including surface wrinkling, creasing, and folding,<sup>8-11</sup> depend on sizes and shapes of the samples<sup>8,5,12-14</sup> and can be tailored by imposing the gradients in sample width, thickness, crosslink density, elastic modulus,<sup>23</sup> or by introducing dynamic variations in sample properties or external conditions.<sup>24</sup> Bucking plays an important role in defining shapes and properties of various heterogeneous gel-based systems, from controlling three dimensional shape transformations in thin hydrogel sheets with embedded arrays of stripes<sup>25,26</sup> to buckling-induced interactions between inclusions in the infinite thin plate. 27,28 Buckling-induced

shape morphing of responsive hydrogels or hybrid materials incorporating hydrogels can be achieved by tuning gel properties and external conditions, <sup>29–31</sup> and snap-through buckling can be generated via transient shape changes during the gel drying.<sup>32</sup>

Stimuli-responsive gels undergo extensive volume changes in response to changes in environmental conditions such as temperature, light, and solvent quality. The Further, an applied tension affects volume phase transition in gels: an increase in tension increases the volume phase transition temperature and can result in a shift from the discontinuous to continuous volume phase transitions. While mechanical instabilities may result in transient surface patterns observed during the extensive swelling of gels freely suspended in solvents, these patterns disappear in the absence of constraints upon reaching an equilibrium. In other words, an equilibrium degree

Received: January 15, 2021 Revised: March 24, 2021 Published: April 12, 2021





of swelling corresponding to the selected external conditions is reached within the unconstrained homogeneous sample. If however the swelling is mechanically constrained, the compressive stresses are generated, which in turn may result in differential swelling, local or global buckling, or surface wrinkling or creasing. 40,41 The swelling of a thin hydrogel strip or film may be constrained by either clamping its single edge 40-43 or both edges, 44,45 confining a strip gel in a corona geometry, 41,44 or by bonding a thin polymer layer with higher stiffness to the gel undergoing swelling. In the latter case, if the swelling of the gel layer is constrained by the bonded stiffer polymer layer, the instability arises due to the mismatch between the elastic moduli of two materials. 40,46-49 Notably, the elastic properties of the thermoresponsive hydrogels, such as poly(N-isopropylacrylamide) (PNIPAAm) hydrogels, vary with temperature with higher elastic modulus measured well above the volume phase transition temperature, 50-53 while softening is reported at the phase transition temperatures. 51-53 This temperature dependence of the elastic modulus correspondingly affects the features of the wrinkling patterns observed in the bilayer systems incorporating PNIPAAm.<sup>50</sup> In addition to rather extensively studied bilayer systems, the trilayer hybrids incorporating the thermoresponsive hydrogel layer were recently fabricated; these systems allowed for simultaneous control of the Gaussian curvature and direction of buckling in shape-morphing systems.<sup>54</sup> Finally, buckling of layered hydrogel films constrained at the short edges was used to design a material with negative swelling (i.e., material which shrinks when it imbibes the solvent).<sup>45</sup>

A restriction of swelling of a thin gel strip by clamping its long edge is well known to result in buckling instability if the critical conditions are satisfied.<sup>41</sup> A linear stability analysis using Föppl-von Kármán (FvK) equations<sup>55</sup> allows one to estimate a wavelength of periodic patterns in the samples with the long edge clamped. In the limit of sufficiently thin plates  $(h_0/L \ll 1)$ , the wavelength of sinusoidal buckling is shown to scale linearly with the sample width,  $w_0$ , as  $^{41}$   $\lambda_W^* = 3.26w_0$ . This scaling is in an agreement with the wavelength measured in experiments for the samples of various thicknesses. 41 However, with the increase in the swelling ratio, the wavelengths measured in the experiments may exhibit relatively large deviations from the above scaling. 40 While the linear stability analysis is often used to predict both the threshold of the critical compressive stress that is required for the onset of buckling and the wavelength of patterns formed, the assumptions made during this analysis have the following major limitations: 41 (a) the most unstable modes used to calculate the wavelengths are taken at the instability threshold, while the experimental conditions often correspond to external stresses well above this threshold and (b) the variations in the thickness and in the elastic properties of the plate during swelling are neglected. The above limitations are expected to hold for sufficiently small perturbations, while the patterns observed often have relatively large amplitudes and notable deviations from the constant thickness.

Controlling pattern formation dynamically in synthetic materials would allow one to control a range of functionalities of surfaces and interfaces. Among the potential applications of patterned surfaces are adhesives with controllable strength, self-cleaning surfaces based on delamination, 77,58 and directed waves that can transport cargo. One means of controlling pattern formation is by utilizing chemical reactivity, for example, via chemomechanical coupling in chemoresponsive

gels. <sup>59–64</sup> Chemomechanical self-oscillations were recently reported in gels undergoing dynamic buckling. <sup>65</sup> Mechanical stimuli such as controlled sequential release of prestrain, <sup>66</sup> simple stretching and recovery of bilayers, <sup>50,67</sup> dynamical loading and unloading, <sup>68</sup> longitudinal and/or transverse compression, <sup>69–71</sup> and uniaxial stretching <sup>72</sup> provide effective means of controlling patterns in bilayer systems, elastic plates, and ridges. For example, the sequential release of equi-biaxial prestrain in one direction, followed by the release of strain in another direction results in the transition from the disordered labyrinth to ordered herringbone patterns in polydimethylsiloxane-based bilayers. <sup>66</sup>

Introducing simple means of dynamic control of pattern formation in gel-based systems mechanically by stretching and compression provides means of mechanical control of dynamic compartmentation and topography in these materials, which could further promote their usage in a number of applications. Herein, we demonstrate mechanical control of the out-of-plane deformations of the thin PNIPAAm gel membranes clamped at two long edges. PNIPAAm has a lower critical solution temperature around 32 °C; when PNIPAAm chains are crosslinked, the hydrogel undergoes volume phase transition and deswells at higher temperatures. The absolute value of the volume phase transition temperature depends on the gel properties, such as crosslink density and polymer volume fraction at preparation, <sup>73–75</sup> and external conditions such as an applied external tension. <sup>36–38</sup> Herein, we show that the features of patterns formed dynamically and an onset of pattern formation can be controlled by the strain rate during the stretching and compression.

We model the dynamics of pattern formation in a confined thin PNIPAAm membrane and the dynamics of transitions between the patterns under the mechanical forcing. In what follows, we first characterize equilibrium patterns in our simulations dependent on the depth of the temperature quench. By utilizing three-dimensional simulations capturing constrained swelling of a hydrogel membrane along with the linear stability analysis, we identify the limits of the applicability of the linear stability analysis in predicting characteristic wavelength of these patterns and an onset of buckling. We characterize the deformation of the membrane by calculating the wavelength and the amplitude of the buckling patterns. We then characterize the effect of the stretching and compression of the samples on the out-of-plane deformations of the membrane and characterize hysteresis in the system response to the mechanical forcing.

# MODEL

We use a three-dimensional gel lattice spring model (3D gLSM)<sup>76,77</sup> to carry out simulations of the dynamics of the confined gel membranes. The gLSM was originally developed to simulate dynamics of chemoresponsive gels undergoing self-oscillations; <sup>78,79</sup> it combines the finite element approach for the spatial discretization of the equations of the gel elastodynamics and finite difference approach for the reaction—diffusion equations if reactions take place with the polymer network. <sup>77</sup> The gLSM was used to simulate the dynamics of various chemoresponsive gels and was validated with respect to a number of experimental studies. <sup>61,76,77,80–82</sup> The gLSM has also been extended to simulate dynamics of gel composites with embedded filaments <sup>83,84</sup> or nanoparticles. <sup>85</sup> Within the gLSM, <sup>78</sup> the total energy of the deformed polymer

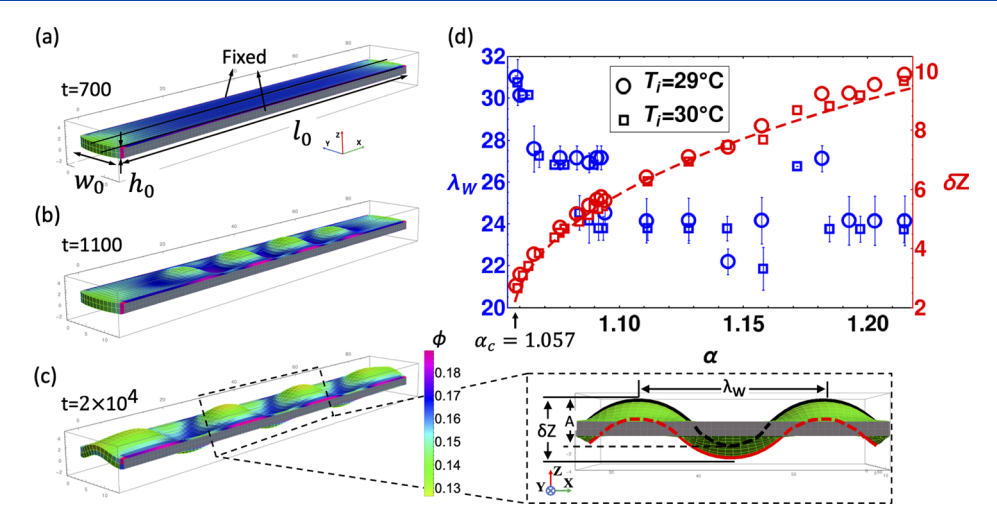


Figure 1. Pattern formation in the constrained gel membrane. (a–c) Morphologies of the sample subjected to the instantaneous temperature quench from 30 to 24 °C at t=700 in (a), t=1100 in (b), and  $t=2\times10^4$  in (c). The color represents the local volume fraction of polymer,  $\phi$ , according to the color bar in (c). The sample is confined at the long edges, as marked in gray. An inset in (c) represents the cross section of the sample taken along the central node in the y-direction. (d) Wavelength  $\lambda_W$  (blue, left axis) and the amplitude  $\delta Z$  (red, right axis) of fully developed patterns as a function of the characteristic swelling ratio  $\alpha$ . The red dashed line is eq 4, where  $\alpha_c = 1.057$ ,  $p_1 = 22.46$ , and  $p_2 = 1.57$ .

matrix comprises the mixing energy,  $U_{\rm mix}$ , and elastic energy,  $U_{\rm el}$ . The dimensionless mixing energy reads  $^{86}$ 

$$U_{\text{mix}} = I_3^{1/2} [(1 - \phi) \ln(1 - \phi) + \chi_{\text{FH}}(\phi, T) \phi (1 - \phi)]$$
(1)

where  $\chi_{\rm FH}(\phi,T)$  is the Flory–Huggins interaction parameter, which depends on the polymer volume fraction  $\phi$  and temperature T, and  $I_3=\det \hat{\bf B}$  is an invariant of the left Cauchy–Green (Finger) strain tensor  $\hat{\bf B}.^{87}~I_3^{1/2}$  represents the change in the volume of the gel relative to its volume in preparation, where  $\phi=\phi_0.^{87}$  The dimensionless elastic energy  $U_{\rm el}$  due to the deformation of the rubber-like cross-linked polymer network is written as  $^{88,89}$ 

$$U_{\rm el} = \frac{c_0}{2} (I_1 - 3 - \ln I_3^{1/2}) \tag{2}$$

The parameter  $c_0 = \nu V_s/N_A$  is a dimensionless crosslink density, where  $\nu$  is the number density of elastically active polymer strands per unit volume at preparation,  $V_s$  is the molar volume of solvent,  $N_A$  is the Avogadro constant, and  $I_1 = \text{tr}\hat{\mathbf{B}}$ . Both energy contributions are normalized by  $k_BT$ , where  $k_B$  is the Boltzmann constant. The dimensionless stress tensor (normalized by  $k_BTN_A/V_s$ ) can be written as  $^{78,79}$   $\hat{\boldsymbol{\sigma}} = -P(\phi,T)$   $\hat{\mathbf{I}} + c_0\phi\phi_0^{-1}\hat{\mathbf{B}}$ , where  $\hat{\mathbf{I}}$  is the unit tensor, and  $P(\phi,T) = \pi_{\text{mix}}(\phi,T) + c_0\phi(2\phi_0)^{-1}$  is the isotropic pressure with  $\pi_{\text{mix}}(\phi,T) = -[\phi + \ln(1-\phi) + \chi\phi^2]$ ,  $\phi_0$  is a polymer volume fraction in preparation, and  $\chi = \chi_{\text{FH}}(\phi,T) - (1-\phi)\partial\chi_{\text{FH}}(\phi,T)/\partial\phi$ . The contributions from elastic and mixing components to a total stress are balanced at equilibrium ( $\hat{\boldsymbol{\sigma}} = 0$ ) so that the equilibrium volume fraction of the polymer in the unconstrained three-dimensional sample,  $\phi_{\text{eq}}(T)$ , can be found at a given temperature T by solving  $T^{76}$ 

$$\pi_{\text{mix}}(\phi_{\text{eq}}, T) = c_0 \left[ \left( \frac{\phi_{\text{eq}}}{\phi_0} \right)^{1/3} - \frac{\phi_{\text{eq}}}{2\phi_0} \right]$$
(3)

The equilibrium degree of swelling is correspondingly calculated as  $\lambda_{\rm eq}(T)=(\phi_0/\phi_{\rm eq}(T))^{1/3}$ . The bulk and shear moduli of the PNIPAAm gel at a given temperature can be

estimated as <sup>52,89-91</sup> 
$$K = \phi \frac{\partial \hat{\sigma}}{\partial \phi}$$
 and 
$$= \left( \frac{\phi_{eq}^2}{1 - \phi_{eq}} - 2\chi_0(T)\phi_{eq}^2 - 3\chi_1\phi_{eq}^3 \right)$$
$$+ c_0 \left[ \frac{\phi_{eq}}{2\phi_0} - \frac{1}{3} \left( \frac{\phi_{eq}}{\phi_0} \right)^{1/3} \right]$$

 $G = c_0(\phi_{\rm eq}/\phi_0)^{1/3}$ , respectively; these expressions are normalized by  $k_{\rm B}TN_{\rm A}/V_{\rm s}$ . Within the gLSM, the dynamics of the polymer network is derived based on the two-fluid model 77,78 and is assumed to be purely relaxational. Further, the hydrodynamic interactions are neglected and the gel dynamics is captured via solvent—polymer interdiffusion 77,78 so that the forces acting on the deformed hydrogel are balanced by the frictional drag of the solvent. For the derivation of the set of dynamic equations for the gLSM in three dimensions, we refer the reader to the original publication. The polymer network within the 3D gLSM framework obeys neo-Hookean elasticity; hence, at sufficiently small strains, the limit of linear elasticity is expected to hold and linear stability analysis can be performed (see below).

The 3D gel sample is represented by  $(L_x-1)\times (L_y-1)\times (L_z-1)$  general linear hexahedral elements, where  $L_i(i=x,y,z)$  is the number of nodes in the *i*-direction. The sample is assumed to be fully immersed in the solvent (water). At the initial temperature  $T_i$ , all the elements of the unconstrained gel sample are identical cubic elements with the dimensionless edge length defined by the equilibrium degree of swelling,  $\lambda_{\rm eq}(T_i)$ , and the polymer volume fraction within each element,  $\phi_{\rm eq}(T_i)$ . In the reference scenario, we restrict the motion of all the nodes at the long edges (these vertical faces are assumed to be grafted to the hard surfaces, as marked in Figure 1a).

We choose simulation parameters based on the available experimental data to capture physical properties of the PNIPAAm gel matrix. We take the polymer–solvent interaction parameter as  $\chi(\phi,T)=\chi_0(T)+\chi_1\phi$ , where  $\chi_0(T)=\delta h-T\delta s/k_BT$ ,  $\chi_1=0.518$ , and  $\delta h=1.246\times 10^{-13}$  erg and  $\delta s=-4.717\times 10^{-16}$  erg/K are the changes in the enthalpy and entropy during the mixing, respectively. With the above choice, the 3D gLSM was shown to accurately reproduce an

analytical solution for both continuous and discontinuous volume phase transitions observed experimentally in gels with corresponding physical properties. 52,94

In the reference case scenario in the simulations below, we set the polymer volume fraction of PNIPAAm gels in preparation at  $\phi_0 = 0.114$ , the dimensional crosslink density at  $c_0 = 4 \times 10^{-3}$ , and choose the sample size of  $105 \times 15 \times 3$ nodes. These reference parameters are used unless specified otherwise. At the initial temperature  $T_i = 30$  °C, an equilibrium degree of swelling is  $\lambda_{eq} = 0.837$ , resulting in the dimensionless initial size of  $87.0 \times 11.7 \times 1.7$ . Taking the dimensionless unit of length in our simulations as  $L_0 = 10 \mu m$ , the above dimensionless size can be related to the dimensional size of  $0.87 \text{ mm} \times 0.12 \text{ mm} \times 0.02 \text{ mm}$ . In addition, a number of simulations were run with extended sample lengths up to a sample size of 200  $\times$  15  $\times$  3 nodes or 166.5  $\times$  11.7  $\times$  1.7 dimensionless units (corresponding to 1.74 mm × 0.12 mm × 0.02 mm) for the reference parameters chosen above. We estimate the characteristic time scale in our simulations by relating the dimensional relaxation time<sup>95</sup> for the cubic sample of linear size equal to the thickness of the gel (0.02 mm) to the dimensionless relaxation time<sup>83</sup> of the same sample calculated from simulations upon temperature decrease from 30 to 20  $^{\circ}$ C. Taking the collective diffusion coefficient for the gel as  $^{96}$  D = 2 $\times$  10<sup>-11</sup> m<sup>2</sup>/s results in the characteristic time scale of  $T_0 = 80$  s. Below, all the dimensionless values of length and time are provided in units of  $L_0$  and  $T_0$ , respectively. The reference value of a constant strain rate is set at  $\dot{\gamma} = 1 \times 10^{-3}$ , which corresponds to  $7.5 \times 10^{-6}$  mm/min. We note that even the fastest rate  $\dot{\gamma}$  considered below ( $\dot{\gamma} = 4 \times 10^{-3}$ ) corresponds to a sufficiently slow motion (slower than the characteristic diffusion time on the corresponding length scale). Finally, we assume that upon the temperature quench, the temperature is equilibrated instantaneously and uniformly within the gel samples of sizes considered herein since the thermal diffusion coefficient of water exceeds the collective diffusion coefficient of the polymer network by approximately 4 orders of magnitude. 96 With the length scale chosen above, the characteristic wavelengths observed in our simulations are on the same length scale as that of buckling patterns observed in prior experimental studies on swollen gels clamped at the single long edge. 40,41 Additional simulation details are provided in Section S1 (Supporting Information).

#### RESULTS AND DISCUSSION

Swelling-Induced Buckling in Constrained Gel Membrane: Dynamics and Equilibrium Properties. In the first series of simulations, we systematically quenched the temperature of the confined gel membrane from  $T_i = 30$  °C to various lower temperatures  $T_{\rm f}$  between 17.5 and 29 °C (Figure 1). Upon the instantaneous temperature quench, the flat gel membrane begins to swell; however, the compression due to the clamped edges does not allow the sample to attain the equilibrium degree of swelling which the sample would have attained in the absence of the confinement,  $\lambda_{eq}(T_f)$ . Hence, the average volume fraction of the polymer within the constrained sample,  $\phi$ , remains higher than that of the corresponding free sample,  $\phi_{\rm eq}$  (Figure S1). An example of pattern development in the confined sample upon a temperature quench from 30 to 24 °C is provided in Figure 1a-c. At early times, the sample swells through the thickness (z-direction) and remains nearly flat. Correspondingly, the volume fraction of the polymer remains nearly uniform along the length of the sample (xdirection) with the exception of the sample ends, which are effectively less constrained (Figure 1a). Upon further swelling, the flat film loses its in-plane stability and small out-of-plane undulations appear close to the center of the sample. At intermediate times, these undulations increase and propagate toward the ends (Figure 1b), resulting in further decrease of the volume fraction of the polymer (color bar in Figure 1). At late times, the out-of-plane motion slows down until the system attains an equilibrium (Figure 1c).

To characterize the membrane deformation, we calculate the amplitude  $\delta Z$  as the distance between the highest and the lowest z-coordinates within the whole sample and the wavelength  $\lambda_{\rm W}$  as the longitudinal distance between the two neighboring peaks (inset in Figure 1c) averaged over the entire sample. The wavelength  $\lambda_{\rm W}$  is calculated provided that two or more wavelengths can fit within the length of the sample, and the amplitude of the surface undulations, A, exceeds a critical small value (Figure S2a). The amplitude  $\delta Z$  is calculated for all samples including an initial flat membrane. Note that the finite length of the sample results in some deviations of the calculated values of  $\lambda_{\rm W}$  for the samples of various lengths depending on the number of half-wavelengths that the samples can accommodate (Figure S3).

The amplitude  $\delta Z$  (red symbols, right axis) and the wavelength  $\lambda_{\rm W}$  (blue symbols, left axis) depend on the ratio of the degree of swelling the gel would have attained during the free swelling in response to the temperature quench from  $T_i$  to  $T_{\rm f}$   $\alpha = \lambda_{\rm eq}(T_{\rm f})/\lambda_{\rm eq}(T_{\rm i})$  (Figure 1d). An increase in  $\alpha$  defines an increase in the compressive stress exerted by the sidewalls. The respective dependences of the characteristic swelling ratio  $\alpha$  on the depth of the temperature quench for the samples initially at 29 and 30 °C are shown in Figure S4. In effect, the compressive stresses exerted on the sample by the confinement can be estimated by considering a free swelling due to the temperature quench followed by an equi-biaxial compression, with the compressive strain defined as  $\varepsilon = \alpha^{-1} - 1$  (see Section S1: C, Supporting Information). It is constructive to characterize pattern formation with respect to the characteristic swelling ratio  $\alpha$  defined above since this value can be calculated analytically for unconstrained samples with various physical properties (eq 3); hence, the pattern features can be predicted depending on the physical properties of the gel and the depth of the temperature quench.

Each data point in Figure 1d corresponds to an independent simulation run, and we probe two initial temperatures, as given in the legend. The values of  $T_i$  define the equilibrium degree of swelling at a given temperature ( $\lambda_{\rm eq}(29~^{\circ}{\rm C})=0.860$  and  $\lambda_{\rm eq}$  $(30 \, ^{\circ}\text{C}) = 0.837$ , respectively), which in turn defines the initial sizes of the samples. We calculate  $\lambda_{\rm W}$  and  $\delta Z$  upon reaching an equilibrium. Our simulations show that for all the cases considered in Figure 1d, the in-plane geometry loses its stability for  $\alpha$  exceeding a critical value,  $\alpha_c = 1.057$ . Our results point out that one could predict an onset of buckling in thin gel membranes confined by the two edges simply based on the ratio between the degrees of swelling of the free samples at the final and initial temperatures,  $\alpha$ . Further increase in  $\alpha$  results in a decrease of the wavelength, followed by its saturation at an approximately constant value (Figure 1d). At higher values of  $\alpha$  considered ( $\alpha \geq 1.18$ ), an increase in the depth of the temperature quench does not change the wavelength but results in the increase of the amplitude,  $\delta Z$ . This behavior is robust and is confirmed in an independent series of simulations for significantly longer samples (Figure S3c). These

simulations show that an increase in  $\alpha$  above the critical value of  $\alpha_c$  results in an increase in the amplitude as

$$\delta Z(\alpha) = p_1 \sqrt{1/\alpha_c - 1/\alpha} + p_2 \tag{4}$$

where  $p_1$  and  $p_2$  are the fitting parameters depending on gel properties (see below). This scaling is similar to the scaling proposed for the postbuckling of elastic plates under uniaxial compression, which shows that the off-plane deflection increases proportionally to the square root of the magnitude of the excess stress relative to the critical compressive stress required for buckling. A similar dependence was reported in previous studies  $^{42,43}$  for the amplitude of swollen gels clamped at a single edge.

In the additional series of simulations, we probed the effect of the gel width  $w_0$  and the dimensionless crosslink density  $c_0$ . We find that the decrease in either  $w_0$  or  $c_0$  results in an increase in  $\alpha_c$  (Figures S5). At  $\alpha$  significantly exceeding a critical value of  $\alpha_c$ ,  $\lambda_W(\alpha)$  and  $\delta Z(\alpha)$  effectively overlap for the samples with different crosslink densities. The values of  $\alpha_c$  found in the simulations and the fitting parameters  $p_1$  and  $p_2$  are provided in Table S1. These results show that an increase in  $w_0$  or a decrease in  $c_0$  results in an increase in  $p_1$ , while the value of  $p_2$  is approximately equal to the average sample thickness at the onset of pattern formation.

While the gel elastodynamics within the gLSM model used herein obeys neo-Hookean elasticity,77,79 in the limit of the small strains, the linear elasticity is expected to hold. The elastic properties of the sample at a given temperature (Young's modulus E and Poisson's ratio  $\nu$ ) can be found from the bulk modulus (K) and shear modulus (G) as  $^{55,89}$  $E = \frac{9KG}{3K+G}$  and  $\nu = \frac{(3K-2G)}{2(3K+G)}$ , respectively. It has been shown that the "dip" in K (referred to as softening) may be observed at volume phase transition temperatures depending on the physical properties of gel. 51-53 The Poisson's ratio calculated from the simulations at small compressive strains is in good agreement with analytical estimates (see Section S1: B and Figure S6). Notably, the functional dependence of the Poisson's ratio on the temperature for the thermoresponsive gels undergoing volume phase transition reproduced in our simulations and low values of  $\nu$  in the vicinity of the phase transitions are in good agreement with corresponding experimental studies. 52,53,100

We perform a linear stability analysis of a thin flat confined hydrogel using FvK equations. These equations are derived based on minimizing the total Hookean elastic energy of a thin plate with a constant thickness.  $^{101,102}$  We assume that the constrained swelling of the gel membranes can be represented via equi-biaxial in-plane compressive strain  $\varepsilon = \alpha^{-1} - 1$  exerted by the confining walls on a sample that was swollen to the final temperature (see Section S1: C and Figure S7a). Notably, a magnitude of the compressive strain was previously correlated with the characteristic swelling ratio to analyze the linear stability of hydrogels with one clamped edge  $^{40,43}$  and swollen layered plates constrained at two short ends.  $^{45}$  Solving FvK equations allows us to find a characteristic wavelength as a function of the sample width  $\lambda_{\rm W}^* \approx 2.62w_0$  and estimate a critical swelling ratio

$$\alpha_{\rm c}^* = \left[1 - \frac{3.09}{1 + \nu} \left(\frac{h_0}{w_0}\right)^2\right]^{-1} \tag{5}$$

corresponding to the onset of instability (details are provided in Section S1: C, Supporting Information). Our analysis shows that a significantly higher critical swelling ratio  $\alpha_c^*$  is required to observe the onset of buckling in the samples with two edges clamped than that for the samples with the single edge clamped. Further, the wavelength estimated analytically for the gel with both long edges constrained is lower than that estimated analytically and observed in experiments for the geometry with one clamped edge,  $\lambda_w^{40,41,43}$  and  $\lambda_w^* \approx 3.26w_0$ . The decrease in the observed equilibrium wavelength for the sample with one clamped edges with respect to that for the sample with one clamped edge was also previously reported in simulations.

In Figure 2a we plot the equilibrium wavelength calculated from the simulations as a function of the sample width  $w_0$  at a

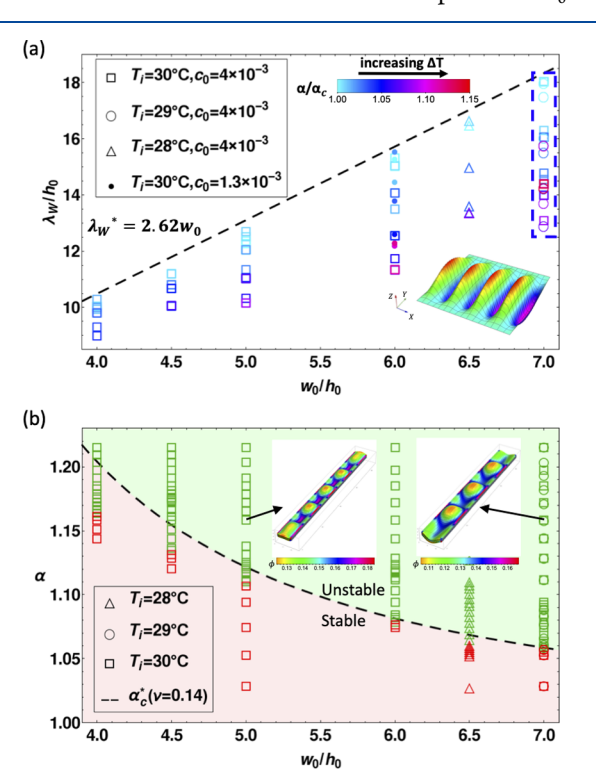


Figure 2. (a) Wavelength  $\lambda_{\rm W}$  at equilibrium as a function of the initial width  $w_0$ . Both  $\lambda_{\rm W}$  and  $w_0$  are normalized by the initial thickness of gels at  $T_v$   $h_0$ . The initial temperature  $T_i$  and the crosslink density  $c_0$  for each independent simulation run (symbols) are given in the legend. The color of the symbols represents the value of the ratio  $\alpha/\alpha_c$ , as shown in the color bar. The dashed line is the analytical prediction from the linear stability analysis,  $\lambda_{\rm W}^*=2.62w_0$ . (b) Stability of the confined sample under various depths of temperature quench in  $(\alpha,w_0/h_0)$  phase space. Independent simulations correspond to three initial temperatures  $T_i$  listed in the legend, and the remaining parameters correspond to the reference parameters (with  $c_0=4\times10^{-3}$ ). Green and red symbols correspond to the buckled and stable flat states, respectively. The dashed line is the analytical prediction of  $\alpha_c^*$  using the linear stability analysis (eq 5). The insets illustrate two fully developed buckled states, as indicated by the arrows.

range of system parameters and compare these simulation values with the predictions from the linear stability analysis (dashed line). Both  $\lambda_{\rm W}$  and  $w_0$  are normalized by the initial thickness of the membrane,  $h_0$ . The inset in the lower right corner shows an ansatz used to solve the corresponding FvK equations (eq S8). The symbols in Figure 2a correspond to the

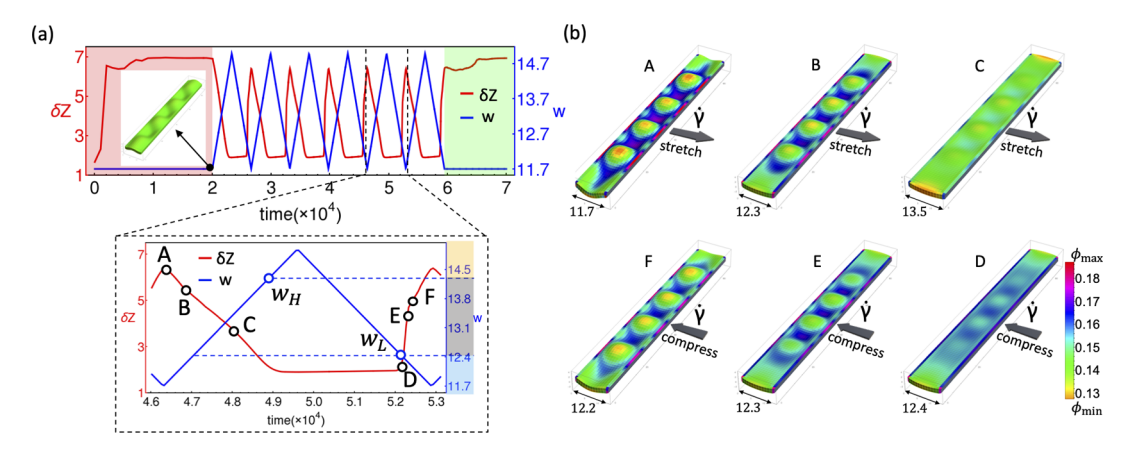


Figure 3. Dynamic reconstruction of buckling patterns upon stretching and compression cycles. (a) Time evolution of the width w (blue, right axis) and the amplitude  $\delta Z$  (red, left axis). The patterns are fully developed following the temperature quench from 30 to 24 °C (red shaded region) before the stretching and compression, with a rate of  $\dot{\gamma} = 1 \times 10^{-3}$  being applied. After the completion of the sixth cycle ( $w = w_0$ ), the sample attains equilibrium (green shaded region). (b) Morphologies of the sample at the time instances marked A–C (stretching) and D–F (compression), as shown in (a). The color represents the local volume fraction of polymer  $\phi$ . The arrows point out the direction of the moving boundary.

simulation data from the samples with various crosslink densities and initial temperatures, as marked in the legend (and hence samples with various initial equilibrium degrees of swelling). The color of the symbols represents  $\alpha/\alpha_c$ , the ratio of  $\alpha$  to the critical value  $\alpha_c$ , which corresponds to the onset of instability in the respective simulation series (the values of  $\alpha_c$  are provided in Table S1). Recall that an increase in  $\alpha$  defines an increase in the compressive stresses exerted by the boundaries due to an increase in the depth of the temperature quench (Figure S4). The data points corresponding to the simulation data in Figure 1d are marked by the blue-dashed rectangle.

Our results show that the equilibrium wavelength  $\lambda_W^*$  calculated from simulations agrees well with the wavelength  $\lambda_W^*$  predicted by the linear stability analysis, provided that an applied temperature quench is close to the onset of instability (symbols in light blue in Figure 2a). As we increase  $\alpha$  above the critical value of  $\alpha_c$ , the analytical predictions overestimate the observed wavelengths, with more pronounced deviations observed for the wider samples. At chosen values of  $\alpha$  and aspect ratios  $w_0/h_0$ , the wavelength normalized by the initial thickness,  $\lambda_W/h_0$ , remains constant as we increase the initial sample thickness  $h_0$  (Figure S8). Finally, the buckling was suppressed in simulations for the samples with  $w_0/h_0 < 4$ ; this is in agreement with prior studies reporting suppression of buckling in narrow samples.  $^{41,44,103}$ 

The stability of the flat confined gel membrane in the phase space of the initial width-to-thickness aspect ratio ( $w_0/h_0$  taken at  $T_{\rm i}$ ) and the characteristic swelling ratio  $\alpha$  is depicted in Figure 2b. The symbols correspond to the simulation data for the three initial temperatures, as listed in the legend. The dashed line corresponds to the analytical prediction from the linear stability analysis,  $\alpha_{\rm c}^*$  (eq 5 and Section S1: C, Supporting Information). We find that the critical values of  $\alpha_{\rm c}$  obtained from our simulations are in a good agreement with analytical predictions for the wider samples but exhibit rather distinct deviations for the narrow samples (small  $w_0/h_0$ ).

To understand the underlying reasons for the deviations observed in simulations with respect to the analytical predictions, recall that the constant thickness and a flat shape are postulated in the linear stability analysis of the flat elastic plate. However, during the gel swelling prior to the

onset of buckling, a notable increase in thickness is observed. Further, since the sidewalls are held stationary, some deviations from the flat shape are also observed due to the swelling through the thickness, while the edges remain constrained. Our simulations show that the increase in the sample thickness at the time instant prior to the onset of buckling with respect to the initial thickness  $h_0$  is more pronounced for the deeper temperature quench (higher values of  $\alpha/\alpha_c$ ) (Figure S9), resulting in larger deviations from the analytical predictions of the characteristic wavelength at higher  $\alpha/\alpha_c$  (Figure 2a). The absolute values of  $\alpha_c$ , however, are higher for the narrow samples, that is, a deeper quench is needed to promote pattern formation in narrow samples. An average increase in the thickness of the sample with respect to the initial thickness at  $\alpha_c$  estimated from the simulation data is ≈21% for the most narrow sample considered and is only around 5% for the widest sample in Figure 2 (Figure S9). As a result, the compression exerted on the sample by the boundaries is underestimated in eq S5, and thereby, the analytical prediction overestimates the onset of instability (a value of  $\alpha_c^*$ ) with more pronounced deviations observed for the narrow samples (small values of  $w_0/h_0$ ).

Dynamic Control of Pattern Formation under Stretching and Compression. We now focus on the dynamic reconstruction of patterns by means of stretching and compression of the buckled sample along its width (ydirection) with a constant strain rate,  $\dot{\gamma}$ . In the scenario depicted in Figure 3a, the sample (the same parameters as in Figure 1c) that had attained an equilibrium after the temperature quench from 30 to 24 °C is subjected to six stretching and compression cycles; the rate is set at  $\dot{\gamma} = 1 \times$ 10<sup>-3</sup> dimensionless units. The red curve in Figure 3a depicts an evolution of the amplitude  $\delta Z$  from the time instant of the temperature quench (t = 0) until the equilibrated patterns are developed (red shaded region), then during the six cycles of stretching and compression, followed by an equilibration upon reaching the original width  $w_0$  after the sixth cycle (green shaded region). Here and below, the compression portion of the cycle is applied to the stretched membrane, that is, the compression effectively represents the controlled release of the additional applied strain until the initial sample width  $w_0$  is reached. The blue curve shows a corresponding time evolution

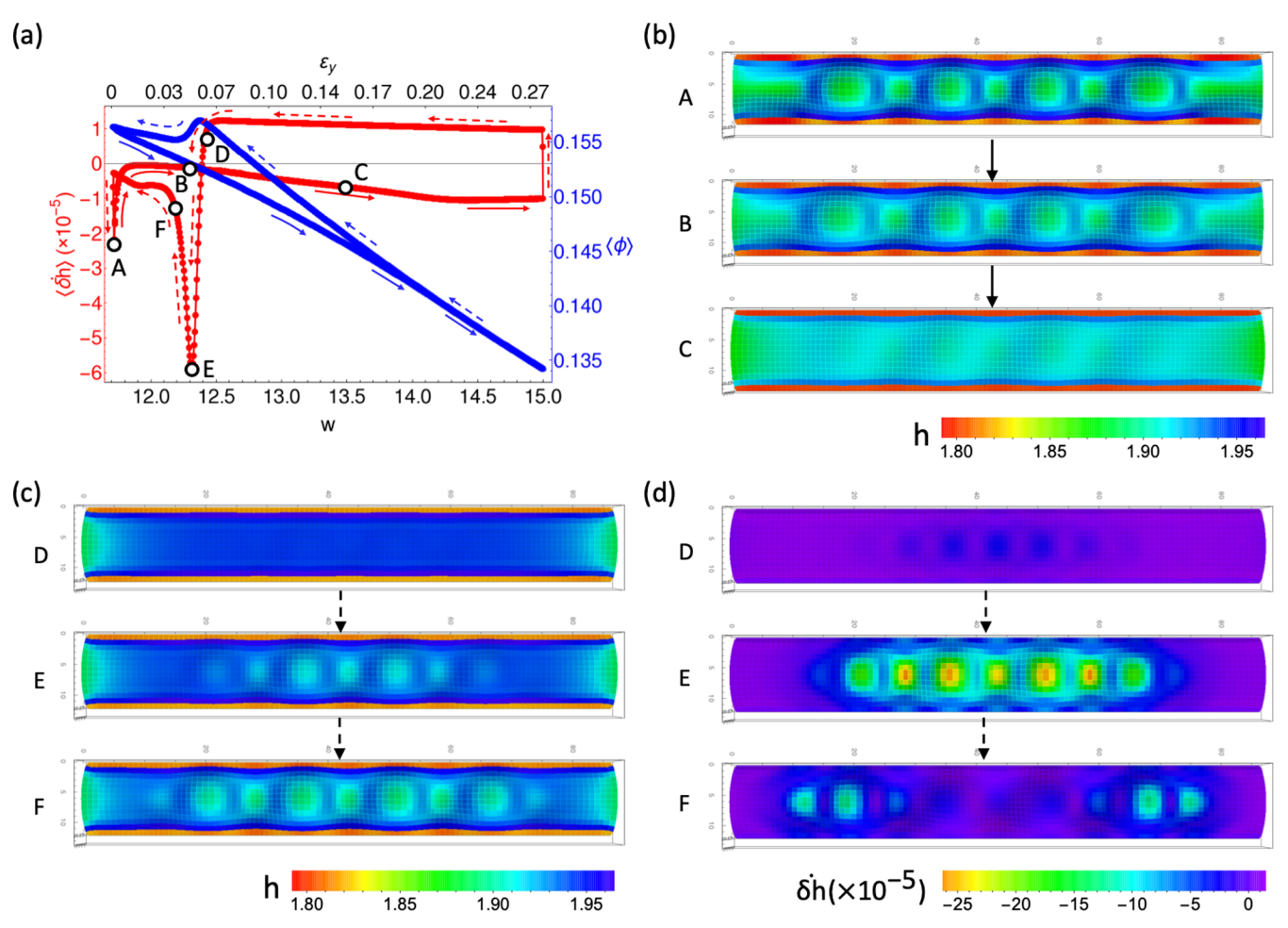


**Figure 4.** Effect of stretching and compression on the thickness of the membrane. (a) Rate of change in the effective average thickness  $\langle \delta \dot{h} \rangle$  (red, left axis) and the average volume fraction of polymer  $\langle \phi \rangle$  (blue, right axis) during an equilibrated stretching and compression cycle. The A–F states correspond to the time instances marked in Figure 3a. The directions of stretching and compression are indicated by the solid and dashed arrows, respectively. (b,c) Sample morphology during stretching [A–F states, as marked in (a), top view], with color representing the local thickness, h. (d) Sample morphology during compression [D–F states as marked in (a), top view], with color representing the local value of  $\delta \dot{h}$ .

of the width of the sample. Excluding the first cycle which has different initial conditions, the dynamics during the remaining cycles is identical (the wavelength and the amplitude during all six cycles are provided in Figure S10).

The inset in Figure 3a shows an evolution during the single cycle and clearly illustrates the asymmetry in  $\delta Z$  during the stretching and compression portions of the cycle; note that the time duration and the rate of the stretching and compression are fixed. Our results show that during the stretching, the patterns are "erased" gradually until the width reaches a critical value denoted as  $w_H$ . During the compression back to the initial width  $w_0$ , the sample remains approximately flat for a prolonged time period until the buckling occurs at  $w_{\rm L}$ , and then, (point D, red curve) the amplitude of patterns formed,  $\delta Z$ , varies significantly faster than that during the stretching portion of the cycle, until the point E on the red curve is reached. With further compression (beyond the point E), an increase in the amplitude  $\delta Z$  noticeably slows down. Our results show that for the sample widths  $w \leq w_L$ , the patterns are observed during both stretching and compression cycles; however, the amplitude can be distinctly different. For the sample widths in the intermediate region,  $w_L < w < w_H$ , the sample remains nearly flat during the compression, while buckling is observed during the stretching. Finally, for  $w \ge w_H$ ,

the buckling patterns are erased and the sample remains approximately flat both during stretching and compression. The sample morphologies during the stretching and compression at selected time instances as marked by A–F in Figure 3a are shown in Figure 3b, where the arrow indicates the moving direction of the confining sidewall.

To further analyze the dynamic response to the stretching and compression, we focus on the variations in the polymer volume fraction,  $\langle \phi \rangle$ , averaged over all the elements, and the average rate of change of the effective thickness of the sample,  $\langle \delta h \rangle$  (Figure 4a). The rate of change of the effective thickness of the sample is calculated as  $\delta h(t) = (h(t)/h(t-\delta t)-1)/\delta t$ , where the effective thickness h(t) is calculated as the difference between the z-coordinates of the respective elements at the top and bottom faces of the sample ((i,j,Lz) and (i,j,0) elements<sup>76</sup>) at times t and  $t - \delta t$  (herein,  $\delta t = 5$ ). While  $\delta h(t)$  and h(t) are calculated in the x-y plane (Figure 4b-d),  $\langle \delta \dot{h} \rangle$  is averaged over the entire sample. The variations in  $\langle \phi \rangle$  and  $\langle \delta h \rangle$  with the sample width during a single cycle (the same cycle as highlighted in the inset in Figure 3a), w, and with effective strain in the y-direction calculated with respect to the initial width,  $w_0$ , as  $\varepsilon_v = w/w_0 - 1$  (upper x-axis) are shown in Figure 4a. The points A-F correspond to the same states as marked in Figure 3; the distributions of  $\delta h$  and h(t) within the sample

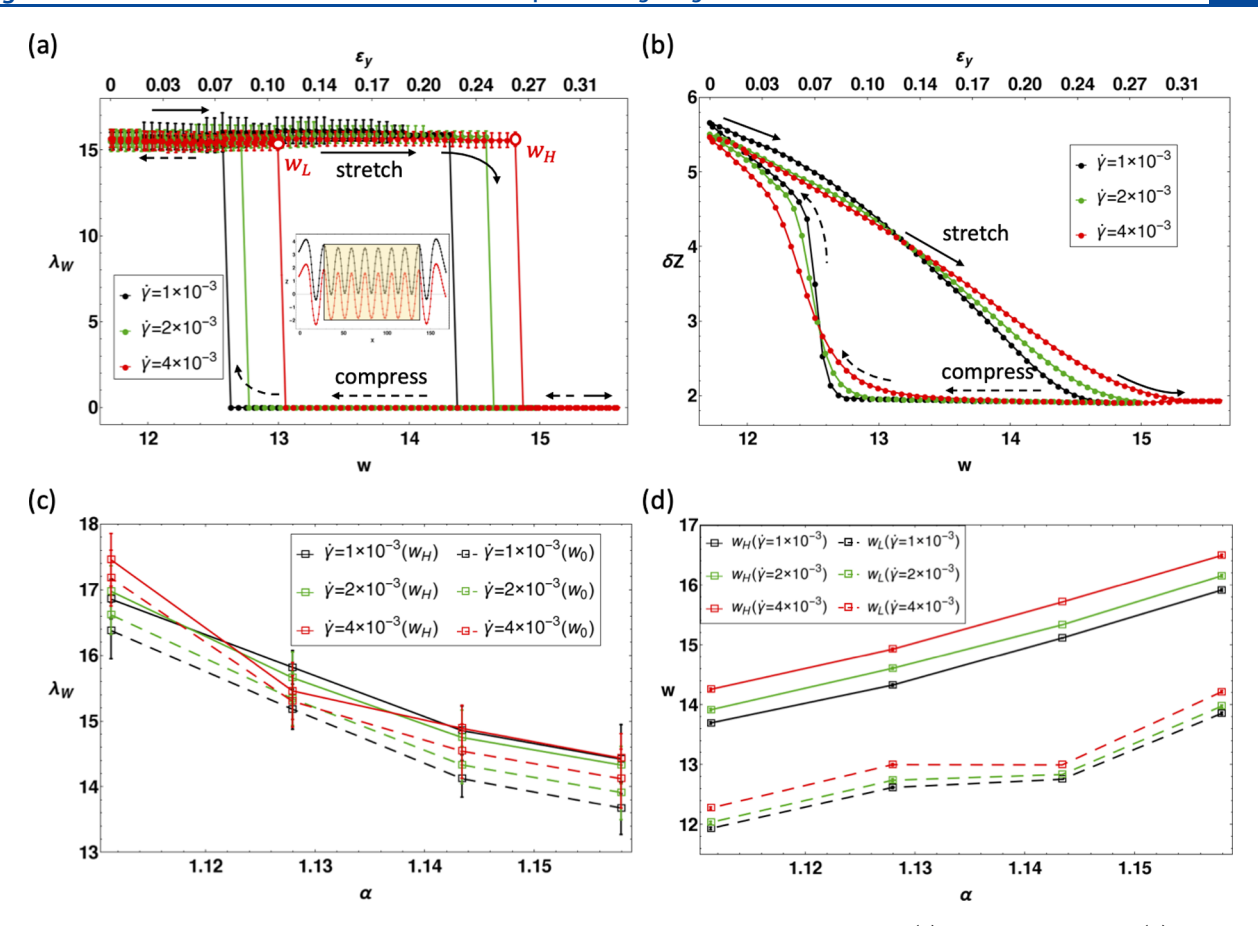


Figure 5. Effects of rates and the depth of the initial temperature quench on pattern reconstruction. (a) Wavelength  $\lambda_W$  and (b) amplitude  $\delta Z$  during an equilibrated cycle; rates are provided in the legend. The stretching and compression are indicated by the solid and dashed arrows, respectively. The inset in (a) shows vertical coordinates of the middle of the top (in black) and bottom (in red) faces of the sample. (c) Wavelength  $\lambda_W$  at  $w = w_H$  and  $w = w_0$  as the function of the characteristic swelling ratio  $\alpha$ . (d) Critical widths,  $w = w_H$  (symbols connected by the solid lines) and  $w = w_L$  (symbols connected by the dashed lines), as a function of the characteristic ratio  $\alpha$ . The error bars in (c) are calculated from data from four equilibrated cycles. The reference parameters are used, including the crosslink density  $c_0 = 4 \times 10^{-3}$  and the initial temperature  $T_i = 30$  °C. The initial sample size is  $166.5 \times 11.7 \times 1.7$ .

(top view) are provided for the same states (Figure 4b-d). These results show that during the stretching portion of the cycle (marked by the solid arrows in Figure 4a), the value of  $\langle \delta \dot{h} \rangle$  (red, left axis) remains negative, indicating the decrease in the effective average film thickness. In addition, the snapshot in Figure S11a shows that the thickness of the sample may increase only locally in selected regions due to pattern restructuring. The values of  $\langle \delta \dot{h} \rangle$  remain negative (i.e., the average membrane thickness decreases during stretching) for all rates considered (Figure S11b). The average polymer volume fraction,  $\langle \phi \rangle$  (blue, right axis), gradually decreases with an increase in w (Figure 4a).

The membrane restructuring process significantly differs for the compression portion of the cycle (indicated by the dashed arrow in Figure 4a). The average thickness of the sample increases during the compression as anticipated as long as the membrane remains approximately flat; the average volume fraction  $\langle \phi \rangle$  during this stage of the compression  $(w \geq w_{\rm L})$  also gradually increases. Following the onset of pattern formation (snapshot D in Figure 4c,d), the  $\delta \dot{h}$  within the small out-ofplane undulations formed at the central region of the sample attains small negative values, while these values are positive within the remainder of the sample (snapshot D, Figure 4d) so that  $\langle \delta \dot{h} \rangle$  remains positive. Further compression results in larger undulations, further extensions out of the plane, and

correspondingly higher negative values of  $\delta h$  within the central region of the membrane (snapshot E in Figure 4d). Upon reaching well-developed patterns at the central portion of the sample (snapshot E), the patterns restructure and the values of  $\delta h$  redistribute accordingly within the sample, with the negative values of  $\delta h$  corresponding to the peaks appearing closer to the ends (snapshot F in Figure 4d). Correspondingly, the effective thickness averaged over the entire sample increases during the compression as long as the sample remains relatively flat but then clearly decreases during pattern restructuring. This observed decrease in the effective thickness of the membrane during compression due to dynamic pattern formation (regions in green in Figures 4d and S12g for the longer samples) indicates that patterns restructuring during compression exhibit some features of behavior rather inherent to mechanical metamaterials, in which unconventional mechanical properties are observed. 104,105

Notably, a time instant marked by E in Figure 4a indicates a transition between the two different regimes discussed: faster increase in  $\delta Z$  corresponding to the pattern formation only in the central region of the membrane and slower increase in  $\delta Z$  corresponding to the pattern reconstruction within the entire sample. Our simulations also show that the sample remains relatively thinner within the hills and valleys of patterns during both compression (Figure 4c) and stretching (Figure 4b).

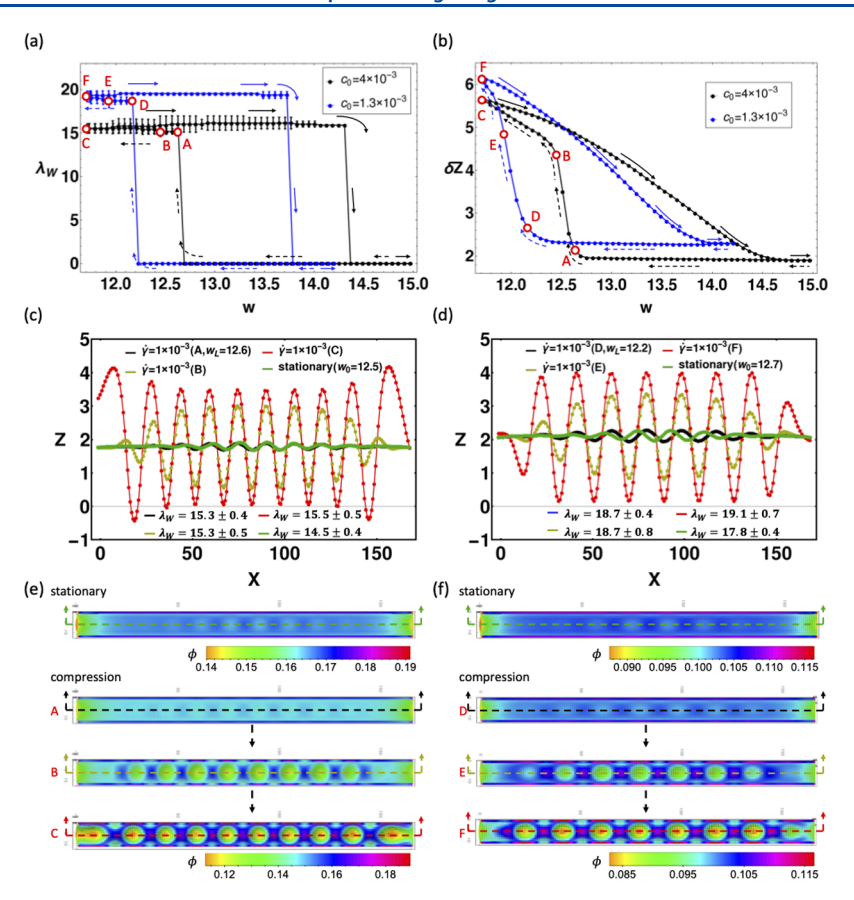


Figure 6. Effects of crosslink density  $c_0$ . (a) Wavelength and (b) amplitude during the equilibrated cycles. The stretching and compression directions are indicated by the solid and dashed arrows, respectively;  $\dot{\gamma} = 1 \times 10^{-3}$  and  $\alpha = 1.128$  for both cases; initial sample sizes are  $166.5 \times 11.7 \times 1.7$  ( $c_0 = 4 \times 10^{-3}$ ) and  $166.9 \times 11.7 \times 2.0$  ( $c_0 = 1.3 \times 10^{-3}$ ). (c,d) Vertical coordinates of the middle of the top face of samples with  $c_0 = 4 \times 10^{-3}$  [in (c)] and  $c_0 = 1.3 \times 10^{-3}$  [in (d)] at A–F states marked in (a,b). For comparison, the vertical coordinates of the middle of the top face of the unstretched samples of matching width (given in the legend) are plotted in (c,d) (green lines). The corresponding wavelengths are listed in the legend. (e,f) Morphologies for the samples with moving boundaries at A–F states marked in (a,b) with color representing the local polymer volume fraction  $\phi$ . Dashed lines indicate the middle of the top face of the samples in (e,f).

Importantly, all the characteristic features of the behavior during the stretching and compression are robust and are also observed in the significantly longer samples (Figure S12).

The snapshots in Figures 4b,c, S11b,c, and S12c,d show that the coordinates of peaks and valleys along the length of the sample remain approximately constant during the stretching and compression, while the amplitude varies significantly. This behavior holds and the wavelength observed remains approximately constant during the stretching and compression cycles for two additional rates  $\dot{\gamma}$  probed (Figure 5a). Notably, the longer samples ( $l_0 = 166.5$ ) are used in Figure 5, and the wavelength is calculated within the shaded region shown in the inset of Figure 5a (see also Figure S3c). The critical width  $w_{\rm H}$ at which the patterns are erased upon the stretching and the critical width  $w_{\rm L}$  at which the onset of pattern formation is observed upon compression, both increase with an increase in the rate  $\dot{\gamma}$  (Figure 5a). We find that the approximately constant wavelength ( $\lambda_{\rm W} \approx 15.3$ ) achieved during the stretching and compression is close to the wavelength at the onset of pattern formation for the sample under the same temperature quench and fixed boundaries (Figure S2b). Our results show that at a range of compression rates considered in Figure 5, the patterns formed at a corresponding critical width,  $w_L$  (characterized by the low value of  $\delta Z$  (Figure 5b), are developing in time with further compression via the increase in the amplitude. In other words, the wavelength prescribed mechanically during the

compression remains constant and does not depend on the variation in the sample width during the compression/stretching cycles, while additional stresses exerted on the membrane during compressions are released via the increase in  $\delta Z$ . The wavelength and the amplitude of patterns accessed dynamically during the stretching and compression significantly differ from those achieved in equilibrium for the confined swollen membrane of the same width. Notably, a significantly smaller wavelength can be accessed dynamically; a comparison between the amplitude  $\delta Z$  and the wavelength  $\lambda_{\rm W}$  of the patterns observed during stretching and compression and those in equilibrium is provided in Figure S10.

Our results show that the hysteresis loop is wider and is shifted toward the larger widths for the samples that undergo stretching and compression at higher rates (Figure 5a). The amplitude  $\delta Z$  (Figure 5b) and the average polymer volume fraction  $\phi$  (not shown) decrease gradually during stretching, confirming that the patterns are erased gradually. The three stages are observed during the compression: at  $w > w_L$ , the samples remain nearly flat, and then, the amplitude  $\delta Z$  increases relatively fast following the onset of buckling ( $w = w_L$ ), with further slower increase in  $\delta Z$  corresponding to pattern reconstruction within the entire sample. These findings suggest that at the strain rates probed in Figure 5a, the patterns do not have sufficient time to restructure longitudinally (despite the motion of the boundary being chosen to be

relatively slow with respect to the characteristic diffusion time on the corresponding length scale even for the highest strain rates considered; see the Model section). To probe the system's response at a significantly lower rate than those chosen in Figure 5a, we run an additional simulation (Figure S13) with  $\dot{\gamma}=5\times10^{-5}$ . These results show that at such slow rates of motion of external boundaries, the wavelength  $\lambda_{\rm W}$  indeed decreases during the stretching and increases during the compression; the coordinates of the peaks and valleys along the length of the sample correspondingly vary dynamically during the stretching and compression (Figure S13c).

In the next series of simulations, we probed the effect of the depth of the initial temperature quench on the sample response during the compression and stretching. We find that an increase in  $\alpha$  results in the decrease of the constant wavelength prescribed during the compression (Figure 5c). Notably, the wavelengths  $\lambda_{\rm W}$  calculated either at  $w_{\rm H}$  (i.e., patterns with the lowest amplitude at the onset of pattern formation) or at  $w_0$  (patterns with the highest amplitude achieved upon compression to the original width) either overlap within the error bar or attain close values at the given value of  $\alpha$ , indicating that the wavelengths remain approximately constant. The error bars in Figure 5c are calculated using the data points from the last four cycles (Figure S12a). Finally, the critical widths  $w_H$  and  $w_L$  both increase with  $\alpha$ , indicating that if a deeper initial temperature quench is applied, the sample needs to be stretched to a larger width prior to erasing the patterns, and the onset of pattern formation is observed at a larger w upon compression. Recall that an increase in  $\alpha$  corresponds to an increase in the effective compression exerted on the sample by the confining boundaries, which is consistent with the observed increase in the critical widths  $w_H$  and  $w_L$ .

Finally, our results in Figure 5 indicate that an approximate value of the wavelength prescribed during the compression can be predicted based on the analysis of the dynamics of pattern development within the samples with stationary boundaries. Specifically, the wavelength observed in Figure 5a is close to the wavelength calculated at early times for the sample at the same temperature quench and a similar width (Figure S2b). Hence, if the wavelength at the onset of pattern formation is predicted from the simulations with the fixed boundaries, one can estimate the wavelength that is prescribed during the compression and stretching. This concept is illustrated for the samples with two crosslink densities (Figure 6). The samples are subjected to six stretching and compression cycles ( $\dot{\gamma} = 1 \times$ 10<sup>-3</sup>) after the patterns fully develop due to the temperature quench corresponding to the same value of the swelling ratio for both examples,  $\alpha = 1.128$ . The dependence of the wavelength during the last cycle on the sample width is shown in Figure 6a. Our results show that the wavelength remains approximately constant for the loosely crosslinked gel ( $\lambda_{\rm W} \approx$ 18.7, in green in Figure 6a), the same as in the reference case scenario (in black in Figure 6a, the same simulation as in Figure 5). Both wavelengths observed during the mechanical forcing are close to those calculated at the onset of buckling for the samples with stationary boundaries and similar widths (green curves in Figure 6c,d for both crosslink densities; corresponding morphologies are shown in top images in Figure 6e,f). Our results also indicate that at a given depth of the temperature quench (given  $\alpha$ ), loosely crosslinked samples exhibit patterns with a larger wavelength  $\lambda_{\rm W}$  and larger  $\delta Z$ , while both critical values  $w_H$  and  $w_L$  decrease (Figure 6a,b).

### CONCLUSIONS

We focus on the dynamics of pattern formation and reconstruction in the confined hydrogel membrane upon the temperature quench and under multiple cycles of stretching and compression. By utilizing three-dimensional simulations capturing constrained swelling of a hydrogel membrane along with the linear stability analysis, we predicted the characteristic wavelength of the patterns formed and critical conditions for the onset of buckling and identified the limits of the applicability of the linear stability analysis. We then characterized the effect of mechanical forcing via stretching and compression on the dynamics of pattern formations. We demonstrate highly asymmetric response of the constrained membrane during stretching and compression and characterize the hysteresis behavior in these systems. Our results show that at a range of the strain rates probed, the wavelength prescribed during the compression remains constant and independent of the sample widths, while the amplitude is regulated by the width. Notably, we demonstrate that significantly smaller wavelengths can be accessed dynamically under mechanical forcing than those achieved in equilibrium in the same systems. We also isolated conditions at which an effective membrane thickness decreases during compression due to dynamic pattern formation and out-of-plane restructuring. Further, while in our studies we choose PNIPAAm gels, we anticipate that similar mechanical adaptation can be observed under mechanical forcing of various gels undergoing swelling under similar dynamic constraints, for example, for poly(N-vinylcaprolactam) gels, which exhibit volume phase transitions nearly identical to that in PNIPAAm gels.<sup>10</sup>

To summarize, we demonstrate that pattern formation in confined hydrogel membranes can be controlled dynamically by mechanical forcing. Hence, our results point out that the surface topography, degree of swelling, and correspondingly, the spatial localization of the effective dynamic compartments within the polymer network can be regulated mechanically by adjusting the rate of stretching and compression, providing simple means of controlling functionality of soft structured gelbased interfaces for a plethora of applications.

# ASSOCIATED CONTENT

# Supporting Information

The Supporting Information is available free of charge at https://pubs.acs.org/doi/10.1021/acs.langmuir.1c00138.

Additional simulations details; dependence of Poisson's ratio of PNIPAAm gels on temperature; linear stability analysis; effects of the sample size on patterns in equilibrium and under stretching and compression; dependence of the characteristic ratio  $\alpha$  on the depth of temperature quench; and dynamics at the low strain rate (PDF)

# AUTHOR INFORMATION

# **Corresponding Author**

Olga Kuksenok — Department of Materials Science and Engineering, Clemson University, Clemson, South Carolina 29634, United States; orcid.org/0000-0002-1895-5206; Email: okuksen@clemson.edu

#### Author

Yao Xiong — Department of Materials Science and Engineering, Clemson University, Clemson, South Carolina 29634, United States

Complete contact information is available at: https://pubs.acs.org/10.1021/acs.langmuir.1c00138

#### **Notes**

The authors declare no competing financial interest.

### ACKNOWLEDGMENTS

This work was supported in part by the National Science Foundation EPSCoR Program under NSF Award no. OIA-1655740. Any opinions, findings, and conclusions or recommendations expressed in this material are those of the author(s) and do not necessarily reflect those of the National Science Foundation. The authors thank Ulf D. Schiller for valuable discussions. Clemson University is acknowledged for generous allotment of compute time on the Palmetto cluster.

# REFERENCES

- (1) Shyer, A. E.; Tallinen, T.; Nerurkar, N. L.; Wei, Z.; Gil, E. S.; Kaplan, D. L.; Tabin, C. J.; Mahadevan, L. Villification: How the Gut Gets Its Villi. *Science* **2013**, 342, 212–218.
- (2) Green, P.; Steele, C. S.; Rennich, S. C. Phyllotactic patterns: A biophysical mechanism for their origin. *Ann. Bot.* **1996**, *77*, 515–528.
- (3) Liu, Z.; Swaddiwudhipong, S.; Hong, W. Pattern formation in plants via instability theory of hydrogels. *Soft Matter* **2013**, *9*, 577–587.
- (4) Wu, D.; Song, J.; Zhai, Z.; Hua, M.; Kim, C.; Frenkel, I.; Jiang, H.; He, X. Visualizing Morphogenesis through Instability Formation in 4-D Printing. ACS Appl. Mater. Interfaces 2019, 11, 47468–47475.
- (5) Tokudome, Y.; Kuniwaki, H.; Suzuki, K.; Carboni, D.; Poologasundarampillai, G.; Takahashi, M. Thermoresponsive Wrinkles on Hydrogels for Soft Actuators. *Adv. Mater. Interfaces* **2016**, 3, 1500802.
- (6) Guvendiren, M.; Burdick, J. A.; Yang, S. Solvent induced transition from wrinkles to creases in thin film gels with depth-wise crosslinking gradients. *Soft Matter* **2010**, *6*, 5795–5801.
- (7) Chan, H. F.; Zhao, R.; Parada, G. A.; Meng, H.; Leong, K. W.; Griffith, L. G.; Zhao, X. Folding artificial mucosa with cell-laden hydrogels guided by mechanics models. *Proc. Natl. Acad. Sci. U.S.A.* **2018**, *115*, 7503–7508.
- (8) Li, B.; Cao, Y.-P.; Feng, X.-Q.; Gao, H. Mechanics of morphological instabilities and surface wrinkling in soft materials: a review. *Soft Matter* **2012**, *8*, 5728–5745.
- (9) Wang, Q.; Zhao, X. Beyond wrinkles: Multimodal surface instabilities for multifunctional patterning. MRS Bull. **2016**, 41, 115–122.
- (10) Wang, Q.; Zhao, X. A three-dimensional phase diagram of growth-induced surface instabilities. Sci. Rep. 2015, 5, 8887.
- (11) Chen, D.; Yoon, J.; Chandra, D.; Crosby, A. J.; Hayward, R. C. Stimuli-Responsive Buckling Mechanics of Polymer Films. *J. Polym. Sci., Polym. Phys.* **2014**, *52*, 1441–1461.
- (12) Dortdivanlioglu, B.; Linder, C. Diffusion-driven swelling-induced instabilities of hydrogels. *J. Mech. Phys. Solid.* **2019**, *125*, 38–52.
- (13) Lestringant, C.; Maurini, C.; Lazarus, A.; Audoly, B. Buckling of an Elastic Ridge: Competition between Wrinkles and Creases. *Phys. Rev. Lett.* **2017**, *118*, 165501.
- (14) Lee, H.; Zhang, J. P.; Jiang, H. Q.; Fang, N. X. Prescribed Pattern Transformation in Swelling Gel Tubes by Elastic Instability. *Phys. Rev. Lett.* **2012**, *108*, 214304.
- (15) Kim, D.; Beebe, D. J. Hydrogel-based reconfigurable components for microfluidic devices. *Lab Chip* **2007**, *7*, 193–198.

- (16) Schedl, A. E.; Neuber, C.; Fery, A.; Schmidt, H.-W. Controlled Wrinkling of Gradient Metal Films. *Langmuir* **2018**, *34*, 14249–14253.
- (17) Schleifer, J.; Marthelot, J.; Jones, T. J.; Brun, P.-T. The fingerprint of a flow: wrinkle patterns in nonuniform coatings on prestretched soft foundations. *Soft Matter* **2019**, *15*, 1405–1412.
- (18) Wu, K.; Yuan, H. Z.; Li, S. J.; Zhang, J. Y.; Liu, G.; Sun, J. Two-stage wrinkling of Al films deposited on polymer substrates. *Scripta Mater.* **2019**, *162*, 456–459.
- (19) Lim, J.; Choi, S.-J.; Kim, P. Controlling Wrinkle Propagation in the Bilayer System with Thickness-Gradient. *Adv. Mater. Interfaces* **2018**, *5*, 1701109.
- (20) Zhou, Y.; Duque, C. M.; Santangelo, C. D.; Hayward, R. C. Biasing Buckling Direction in Shape-Programmable Hydrogel Sheets with Through-Thickness Gradients. *Adv. Funct. Mater.* **2019**, 29, 1905273.
- (21) Guvendiren, M.; Yang, S.; Burdick, J. A. Swelling-Induced Surface Patterns in Hydrogels with Gradient Crosslinking Density. *Adv. Funct. Mater.* **2009**, *19*, 3038–3045.
- (22) de Haan, L. T.; Willigers, T. J. J.; Wijkhuijs, L. E. A.; Hendrikx, M.; Nguyen, C. T.; Leclère, P.; Souren, A. E. J.; Zhou, G.; Debije, M. G. Contactless Control of Local Surface Buckling in Photoaligned Gold/Liquid Crystal Polymer Bilayers. *Langmuir* **2018**, *34*, 10543–10549.
- (23) Lei, X.; Ye, D.; Chen, J.; Tang, S.; Sun, P.; Chen, L.; Lu, A.; Du, Y.; Zhang, L. Customizable Multidimensional Self-Wrinkling Structure Constructed via Modulus Gradient in Chitosan Hydrogels. *Chem. Mater.* **2019**, *31*, 10032–10039.
- (24) Hou, H.; Yin, J.; Jiang, X. Smart Patterned Surface with Dynamic Wrinkles. *Acc. Chem. Res.* **2019**, *52*, 1025–1035.
- (25) Wu, Z. L.; Moshe, M.; Greener, J.; Therien-Aubin, H.; Nie, Z.; Sharon, E.; Kumacheva, E. Three-dimensional shape transformations of hydrogel sheets induced by small-scale modulation of internal stresses. *Nat. Commun.* **2013**, *4*, 1586.
- (26) Thérien-Aubin, H.; Moshe, M.; Sharon, E.; Kumacheva, E. Shape transformations of soft matter governed by bi-axial stresses. *Soft Matter* **2015**, *11*, 4600–4605.
- (27) Oshri, O.; Biswas, S.; Balazs, A. C. Modeling the behavior of inclusions in circular plates undergoing shape changes from two to three dimensions. *Phys. Rev. E* **2019**, *100*, 043001.
- (28) Oshri, O.; Biswas, S.; Balazs, A. C. Buckling-induced interaction between circular inclusions in an infinite thin plate. *Phys. Rev. E* **2020**, 102, 033004.
- (29) Jeon, S.-J.; Hauser, A. W.; Hayward, R. C. Shape-Morphing Materials from Stimuli-Responsive Hydrogel Hybrids. *Acc. Chem. Res.* **2017**, *50*, 161–169.
- (30) Kim, J.; Hanna, J. A.; Byun, M.; Santangelo, C. D.; Hayward, R. C. Designing Responsive Buckled Surfaces by Halftone Gel Lithography. *Science* **2012**, *335*, 1201–1205.
- (31) Hauser, A. W.; Evans, A. A.; Na, J.-H.; Hayward, R. C. Photothermally Reprogrammable Buckling of Nanocomposite Gel Sheets. *Angew. Chem., Int. Ed.* **2015**, *54*, 5434–5437.
- (32) Kim, Y.; van den Berg, J.; Crosby, A. J. Autonomous snapping and jumping polymer gels. *Nat. Mater.* **2021**, DOI: 10.1038/s41563-020-00909-w.
- (33) Chatterjee, S.; Hui, P.; Kan, C.-w. Thermoresponsive Hydrogels and Their Biomedical Applications: Special Insight into Their Applications in Textile Based Transdermal Therapy. *Polymers* **2018**, *10*, 480.
- (34) Li, L.; Scheiger, J. M.; Levkin, P. A. Design and Applications of Photoresponsive Hydrogels. *Adv. Mater.* **2019**, *31*, 1807333.
- (35) Rizwan, M.; Yahya, R.; Hassan, A.; Yar, M.; Azzahari, A. D.; Selvanathan, V.; Sonsudin, F.; Abouloula, C. N. pH Sensitive Hydrogels in Drug Delivery: Brief History, Properties, Swelling, and Release Mechanism, Material Selection and Applications. *Polymers* 2017, 9, 137.
- (36) Takigawa, T.; Takakura, Y.; Masuda, T. Volume phase transition of a poly(N-isopropylacrylamide) gel under tension. Emergence of a new critical point. *Polym. J.* **2001**, *33*, 909–911.

- (37) Dušková-Smrčková, M.; Dusek, K. How to Force Polymer Gels to Show Volume Phase Transitions. *ACS Macro Lett.* **2019**, *8*, 272–278.
- (38) Hirotsu, S.; Onuki, A. Volume Phase-Transition of Gels under Uniaxial Tension. *J. Phys. Soc. Jpn.* **1989**, *58*, 1508–1511.
- (39) Tanaka, T.; Sun, S.-T.; Hirokawa, Y.; Katayama, S.; Kucera, J.; Hirose, Y.; Amiya, T. Mechanical Instability of Gels at the Phase-Transition. *Nature* **1987**, 325, 796–798.
- (40) DuPont, S. J.; Cates, R. S.; Stroot, P. G.; Toomey, R. Swelling-induced instabilities in microscale, surface-confined poly(N-isopropylacryamide) hydrogels. *Soft Matter* **2010**, *6*, 3876–3882.
- (41) Mora, T.; Boudaoud, A. Buckling of swelling gels. *Eur. Phys. J. E* **2006**, *20*, 119–124.
- (42) Tirumala, V. R.; Stafford, C. M.; Ocola, L. E.; Douglas, J. F.; Mahadevan, L. Geometric Control of Rippling in Supported Polymer Nanolines. *Nano Lett.* **2012**, *12*, 1516–1521.
- (43) Jiang, R.; Xiao, J.; Song, J. Buckling of thin gel strip under swelling. Theor. Appl. Mech. Lett. 2017, 7, 134–137.
- (44) Liu, Z.; Hong, W.; Suo, Z.; Swaddiwudhipong, S.; Zhang, Y. Modeling and simulation of buckling of polymeric membrane thin film gel. *Comput. Mater. Sci.* **2010**, *49*, S60–S64.
- (4S) Liu, J.; Gu, T.; Shan, S.; Kang, S. H.; Weaver, J. C.; Bertoldi, K. Harnessing Buckling to Design Architected Materials that Exhibit Effective Negative Swelling. *Adv. Mater.* **2016**, 28, 6619–6624.
- (46) Dervaux, J.; Amar, M. B. Mechanical Instabilities of Gels. *Annu. Rev. Condens. Matter Phys.* **2012**, *3*, 311–332.
- (47) Zhou, Z.; Li, Y.; Guo, T.; Guo, X.; Tang, S. Surface Instability of Bilayer Hydrogel Subjected to Both Compression and Solvent Absorption. *Polymers* **2018**, *10*, 624.
- (48) Kato, M.; Asoh, T. A.; Uyama, H. Hydrogel Adhesion by Wrinkling Films. *Macromol. Rapid Commun.* **2019**, 40, 1900434.
- (49) Auguste, A.; Jin, L.; Suo, Z.; Hayward, R. C. Post-wrinkle bifurcations in elastic bilayers with modest contrast in modulus. *Extrem. Mech. Lett.* **2017**, *11*, 30–36.
- (50) Kato, M.; Kashihara, Y.; Asoh, T.-A.; Uyama, H. Geometry Control of Wrinkle Structures Aligned on Hydrogel Surfaces. *Langmuir* **2020**, *36*, 1467–1473.
- (S1) Sierra-Martin, B.; Laporte, Y.; South, A. B.; Lyon, L. A.; Fernandez-Nieves, A. Bulk modulus of poly(N-isopropylacrylamide) microgels through the swelling transition. *Phys. Rev. E* **2011**, *84*, 011406.
- (52) Hirotsu, S. Softening of Bulk Modulus and Negative Poisson Ratio near the Volume Phase-Transition of Polymer Gels. *J. Chem. Phys.* **1991**, *94*, 3949–3957.
- (53) Voudouris, P.; Florea, D.; van der Schoot, P.; Wyss, H. M. Micromechanics of temperature sensitive microgels: dip in the Poisson ratio near the LCST. *Soft Matter* **2013**, *9*, 7158–7166.
- (54) Jeon, S.-J.; Hayward, R. C. Simultaneous control of Gaussian curvature and buckling direction by swelling of asymmetric trilayer hydrogel hybrids. *Soft Matter* **2020**, *16*, 688–694.
- (55) Landau, L. D.; Lifshitz, E. M. *Theory of Elasticity*, 3rd ed.; Butterworth-Heinemann, 1986; p 196.
- (56) Chan, E. P.; Smith, E. J.; Hayward, R. C.; Crosby, A. J. Surface wrinkles for smart adhesion. *Adv. Mater.* **2008**, 20, 711–716.
- (57) Pocivavsek, L.; Ye, S.-H.; Pugar, J.; Tzeng, E.; Cerda, E.; Velankar, S.; Wagner, W. R. Active wrinkles to drive self-cleaning: A strategy for anti-thrombotic surfaces for vascular grafts. *Biomaterials* **2019**, *192*, 226–234.
- (58) Pocivavsek, L.; Pugar, J.; O'Dea, R.; Ye, S.-H.; Wagner, W.; Tzeng, E.; Velankar, S.; Cerda, E. Topography-driven surface renewal. *Nat. Phys.* **2018**, *14*, 948–953.
- (59) Yoshida, R. Self-Oscillating Gels Driven by the Belousov-Zhabotinsky Reaction as Novel Smart Materials. *Adv. Mater.* **2010**, 22, 3463–3483.
- (60) Epstein, I. R.; Vanag, V. K.; Balazs, A. C.; Kuksenok, O.; Dayal, P.; Bhattacharya, A. Chemical Oscillators in Structured Media. *Acc. Chem. Res.* **2012**, *45*, 2160–2168.

- (61) Chen, I. C.; Kuksenok, O.; Yashin, V. V.; Moslin, R. M.; Balazs, A. C.; Van Vliet, K. J. Shape- and size-dependent patterns in self-oscillating polymer gels. *Soft Matter* **2011**, *7*, 3141–3146.
- (62) Ren, L.; Yuan, L.; Gao, Q.; Teng, R.; Wang, J.; Epstein, I. R. Chemomechanical origin of directed locomotion driven by internal chemical signals. *Sci. Adv.* **2020**, *6*, No. eaaz9125.
- (63) Ren, L.; Wang, L.; Gao, Q.; Teng, R.; Xu, Z.; Wang, J.; Pan, C.; Epstein, I. R. Programmed Locomotion of an Active Gel Driven by Spiral Waves. *Angew. Chem., Int. Ed.* **2020**, *59*, 7106–7112.
- (64) Kuksenok, O.; Balazs, A. C. Modeling the Photoinduced Reconfiguration and Directed Motion of Polymer Gels. *Adv. Funct. Mater.* **2013**, 23, 4601–4610.
- (65) Hua, M.; Kim, C.; Du, Y.; Wu, D.; Bai, R.; He, X. Swaying gel: chemo-mechanical self-oscillation based on dynamic buckling. *Matter* **2021**, *4*, 1029.
- (66) Yin, J.; Yagüe, J. L.; Eggenspieler, D.; Gleason, K. K.; Boyce, M. C. Deterministic Order in Surface Micro-Topologies through Sequential Wrinkling. *Adv. Mater.* **2012**, *24*, 5441–5446.
- (67) Wang, C.; Yang, S.; Guo, Q.; Xu, L.; Xu, Y.; Qiu, D. Wrinkled double network hydrogel via simple stretch-recovery. *Chem. Commun.* **2020**, *56*, 13587–13590.
- (68) Jin, L.; Takei, A.; Hutchinson, J. W. Mechanics of wrinkle/ridge transitions in thin film/substrate systems. *J. Mech. Phys. Solid.* **2015**, *81*, 22–40.
- (69) Rhee, D.; Lee, W.-K.; Odom, T. W. Crack-Free, Soft Wrinkles Enable Switchable Anisotropic Wetting. *Angew. Chem., Int. Ed.* **2017**, 56, 6523–6527.
- (70) Audoly, B.; Roman, B.; Pocheau, A. Secondary buckling patterns of a thin plate under in-plane compression. *Eur. Phys. J. B* **2002**, 27, 7–10.
- (71) Zhao, Y.; Shao, Z.-C.; Li, G.-Y.; Zheng, Y.; Zhang, W.-Y.; Li, B.; Cao, Y.; Feng, X.-Q. Edge wrinkling of a soft ridge with gradient thickness. *Appl. Phys. Lett.* **2017**, *110*, 231604.
- (72) Lucantonio, A.; Roché, M.; Nardinocchi, P.; Stone, H. A. Buckling dynamics of a solvent-stimulated stretched elastomeric sheet. *Soft Matter* **2014**, *10*, 2800–2804.
- (73) Zhang, Y.; Furyk, S.; Sagle, L. B.; Cho, Y.; Bergbreiter, D. E.; Cremer, P. S. Effects of Hofmeister anions on the LCST of PNIPAM as a function of molecular weight. *J. Phys. Chem. C* **2007**, *111*, 8916–8924.
- (74) Jain, K.; Vedarajan, R.; Watanabe, M.; Ishikiriyama, M.; Matsumi, N. Tunable LCST behavior of poly(N-isopropylacrylamide/ionic liquid) copolymers. *Polym. Chem.* **2015**, *6*, 6819–6825.
- (75) Lopez, C. G.; Richtering, W. Does Flory-Rehner theory quantitatively describe the swelling of thermoresponsive microgels? *Soft Matter* **2017**, *13*, 8271–8280.
- (76) Kuksenok, O.; Yashin, V. V.; Balazs, A. C. Three-dimensional model for chemoresponsive polymer gels undergoing the Belousov-Zhabotinsky reaction. *Phys. Rev. E* **2008**, *78*, 041406.
- (77) Yashin, V. V.; Kuksenok, O.; Balazs, A. C. Modeling autonomously oscillating chemo-responsive gels. *Prog. Polym. Sci.* **2010**, *35*, 155–173.
- (78) Yashin, V. V.; Balazs, A. C. Theoretical and computational modeling of self-oscillating polymer gels. *J. Chem. Phys.* **2007**, *126*, 124707.
- (79) Yashin, V. V.; Balazs, A. C. Pattern formation and shape changes in self-oscillating polymer gels. *Science* **2006**, *314*, 798–801.
- (80) Yoshida, R.; Tanaka, M.; Onodera, S.; Yamaguchi, T.; Kokufuta, E. In-phase synchronization of chemical and mechanical oscillations in self-oscillating gels. *J. Phys. Chem. A* **2000**, *104*, 7549–7555.
- (81) Kuksenok, O.; Yashin, V. V.; Kinoshita, M.; Sakai, T.; Yoshida, R.; Balazs, A. C. Exploiting gradients in cross-link density to control the bending and self-propelled motion of active gels. *J. Mater. Chem.* **2011**, *21*, 8360–8371.
- (82) Yuan, P.; Kuksenok, O.; Gross, D. E.; Balazs, A. C.; Moore, J. S.; Nuzzo, R. G. UV patternable thin film chemistry for shape and functionally versatile self-oscillating gels. *Soft Matter* **2013**, *9*, 1231–1243.

- (83) He, X.; Aizenberg, M.; Kuksenok, O.; Zarzar, L. D.; Shastri, A.; Balazs, A. C.; Aizenberg, J. Synthetic homeostatic materials with chemo-mechano-chemical self-regulation. *Nature* **2012**, 487, 214–218.
- (84) Kuksenok, O.; Balazs, A. C. Stimuli-responsive behavior of composites integrating thermo-responsive gels with photo-responsive fibers. *Mater. Horiz.* **2016**, *3*, 53–62.
- (85) Savchak, O.; Morrison, T.; Kornev, K. G.; Kuksenok, O. Controlling deformations of gel-based composites by electromagnetic signals within the GHz frequency range. *Soft Matter* **2018**, *14*, 8698–8708
- (86) Hill, T. L. An Introduction to Statistical Thermodynamics; Addison-Weley: Reading, MA, 1960; p 544.
- (87) Atkin, R. J.; Fox, N. An Introduction to the Theory of Elasticity; Longman: New York, 1980; p 272.
- (88) Mark, J. E.; Erman, B. Rubberlike Elasticity: A Molecular Primer, 2nd ed.; Cambridge University Press, 2007; p 272.
- (89) Doi, M. Soft Matter Physics; Oxford University Press, 2013; p 272.
- (90) Rubinstein, M.; Colby, R. H. Polymer Physics; Oxford University Press, 2003; p 454.
- (91) Treloar, L. R. G. The Physics of Rubber Elasticity, 3rd ed.; Oxford University Press, 2005; p 310.
- (92) Doi, M. Effects of Viscoelasticity on Polymer Diffusion. *Springer Proc. Phys.* **1990**, *52*, 100–112.
- (93) Barrière, B.; Leibler, L. Kinetics of solvent absorption and permeation through a highly swellable elastomeric network. *J. Polym. Sci., Polym. Phys.* **2003**, *41*, 166–182.
- (94) Xiong, Y.; Dayal, P.; Balazs, A. C.; Kuksenok, O. Phase Transitions and Pattern Formation in Chemo-Responsive Gels and Composites. *Isr. J. Chem.* **2018**, *58*, 693–705.
- (95) Li, Y.; Tanaka, T. Kinetics of Swelling and Shrinking of Gels. *J. Chem. Phys.* **1990**, 92, 1365–1371.
- (96) Hirose, H.; Shibayama, M. Kinetics of Volume Phase Transition in Poly(N-isopropylacrylamide-co-acrylic acid) Gels. *Macromolecules* **1998**, *31*, 5336–5342.
- (97) Suzuki, A.; Tanaka, T. Phase-Transition in Polymer Gels Induced by Visible-Light. *Nature* **1990**, *346*, 345–347.
- (98) Mansfield, E. H. The Bending and Stretching of Plates, 2nd ed.; Cambridge University Press: Cambridge England; New York, 1989; p
- (99) Stein, M. Loads and Deformations of Buckled Rectangular Plates; U.S. Government Printing Office, 1959; p 27.
- (100) Greaves, G. N.; Greer, A. L.; Lakes, R. S.; Rouxel, T. Poisson's ratio and modern materials. *Nat. Mater.* **2011**, *10*, 823–837.
- (101) Kaiser, R.; Montaldi, J. Peyresq Lectures on Nonlinear Phenomena; World Scientific: Singapore, 2000; p 388.
- (102) Fu, Y. B.; Ogden, R. W. Nonlinear Elasticity: Theory and Applications; Cambridge University Press: Cambridge, U.K.; New York, 2001; p 525.
- (103) Kang, M. K.; Huang, R. Swelling-Induced Instability of Substrate-Attached Hydrogel Lines. *Int. J. Appl. Mech. Eng.* **2011**, *03*, 219–233.
- (104) Bertoldi, K.; Vitelli, V.; Christensen, J.; van Hecke, M. Flexible mechanical metamaterials. *Nat. Rev. Mater.* **2017**, *2*, 17066.
- (105) Mullin, T.; Deschanel, S.; Bertoldi, K.; Boyce, M. C. Pattern transformation triggered by deformation. *Phys. Rev. Lett.* **2007**, *99*, 084301.
- (106) Ramos, J.; Imaz, A.; Forcada, J. Temperature-sensitive nanogels: poly(N-vinylcaprolactam) versus poly(N-isopropylacrylamide). *Polym. Chem.* **2012**, *3*, 852–856.